Variable-Stiffness Control of A Dual-Segment Soft Robot Using Depth Vision

Jiewen Lai, *Student Member, IEEE*, Bo Lu, and Henry K. Chu, *Member, IEEE*

***Abstract*—A soft-bodied robot exhibits prominent dexterity due to the soft nature of its material. However, the softness can become a burden when the robot needs to interact with the environment, given that the targeted object is usually much stiffer than the compliant soft robot. A variable-stiffness soft robot, fusing the merits of softness and stiffness, is in favor of many applications, such as robot-assisted minimally invasive surgeries (R-MIS). In this work, we propose a tendon-tensioning method to adaptively control the stiffness of a dual-segment tendon-driven backboneless soft robot based on depth vision. A depth vision-based closed-loop controller is designed for stiffness compensation when the manipulator is subjected to the external load. Experiments were conducted to examine the feasibility and performance of the proposed method. The results confirm our control scheme on the robot with controllability of stiffness up to 132%. Based on our method, the manipulator with an external payload can follow designated trajectories with positioning errors reduced up to 50% comparing to that with open-loop control. Without quantifying the instantaneous stiffness, this work contributes a generalized method for tuning the stiffness of the tendon-driven soft robots in the presence of external disturbances without onboard sensing.**

***Index Terms*—RGB-D Perception, Soft Robot, Soft Robot Materials and Design, Tendon/Wire Mechanism, Visual Servoing.**

I. Introduction

SOFT robots are usually made from soft-touch materials [1]. The motion of the robot manipulator, which has theoretically infinite degrees of freedom (DOF), can be generated by the elastic deformation of the soft body. With multisegment articulated from one to another, the manipulator can work in sinuous surroundings like a snake. The low Young's modulus of soft material endows the robot to interact with humans safely, which is one of the development trends in robotics.

Robot-assisted minimally invasive surgery (R-MIS) involves a lot of interactions between humans (patients) and robots [2], and soft robots become the most promising candidates. For instance, a soft or continuum robotic manipulator can be used as a surgical forceps to manipulate the soft and fragile tissues [2], [3]. To ensure the safety, it is desired that the manipulator can be soft enough to minimize the harm to the anatomical structure in case of collision. On the contrary, the manipulator should provide sufficient stiffness for physical manipulation such as grasping and ablation [4]–[6]. If the manipulator is too soft, undesired deformation during the physical interaction would increase the challenge in controlling the end-effector. Therefore, it leads to a demand for developing variable-stiffness soft robots that can switch from the flexible state to the rigid state, and reversible if needed [7]. A schematic of the variable-stiffness soft robot is given in Fig. 1.

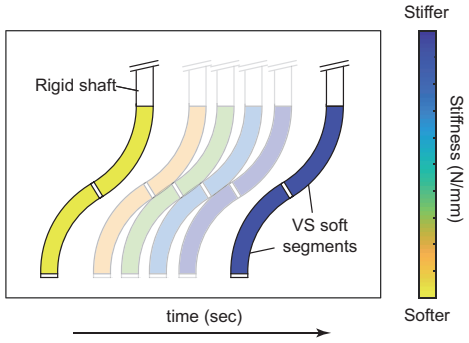

Fig. 1. Conceptual schematic of a variable-stiffness dual-segment soft robot. The manipulator is stiffened with an imperceptible change of its pose.

A. Related Works

In elastic stability theory, the flexural stiffness ($K_b = E_b I$) of a beam can be quantified by the ability to resist bending in *a plane of symmetry* [8]. It can be expressed by the product of the Young's modulus in bending (E_b) and the second moment of area (I). Therefore, varying the stiffness of a soft manipulator basically requires the adjustment on either the material intrinsic properties (E_b) or the structural geometry (I). The employments of changing stiffness by controlling intrinsic material properties in soft robots and biomedical devices have been reported in [9]–[11]. However, the mechanism sacrifices the output force and activation time, which is hence unqualified for the tasks demanding manipulation in a subsecond response.

Aim at developing a variable-stiffness manipulator with fast response, a number of researchers have been working on designing delicate jamming structures for soft/continuum manipulators. The granular jamming mechanism changes the manipulator's stiffness by modifying the interactions of embedded granular particles, e.g., glass beads [12], fiber [13], or even ground coffee [14]. The particles are free-to-flow within the manipulator structure during normal operations, but they

Manuscript received January 19, 2021; revised March 2021; accepted April 2021. This work was supported in part by the Grant 4-RKCM of HK PolyU. *(Corresponding author: Henry K. Chu)*

J. Lai and H. K. Chu are with the Department of Mechanical Engineering, The Hong Kong Polytechnic University, Kowloon, Hong Kong. (email: jw.lai@connect.polyu.hk; henry.chu@polyu.edu.hk).

B. Lu is with the CUHK T Stone Robotics Institute, The Chinese University of Hong Kong, N.T., Hong Kong. (email: bolu@cuhk.edu.hk).

A supplementary video can be found at https://youtu.be/hS9taWGyeVc

Color versions of one or more of the figures in this article are available online at http://ieeexplore.ieee.org.

Digital Object Identifier: see top of this page.

TABLE I
COMPARISON OF VARIABLE-STIFFNESS CONTINUUM MANIPULATORS IN LITERATURE

Continuum Body	Ref.	Body Material(s)	Actuation	Diameter (mm)	Bendable Segments	Stiffening Method
Rigid components	[20]	Ti6Al4V & Steel spring	Cable/Tendon	28	1	Cable tensioning
	[21]	Aluminum & Epoxy	Cable/Tendon	12	1	Cable tensioning
	[22]	3D-printed ABS	Cable/Tendon	20	2	Cable tensioning
	[12]	Granular & Membrane	Pneumatic	15	-	Granular jamming
Soft body	[11]	Silicone	Hydraulic	13 (semicircle)	1	Low-melting-point-alloy
	[13]	Nylon fibers	Pneumatic	16	-	Fiber jamming
	[14]	Silicone & Ground coffee	Hydraulic	25–32	1	Granular jamming
	[15]	Latex rubber & Mylar	Pneumatic	24	1	Layer jamming
	[23]	Silicone (STIFF-FLOP)	Pneumatic & Cable	23	1	Cable tensioning
	Ours	3D-printed elastomer	Cable/Tendon	9	2	Cable tensioning

are interlocked when the vacuum is applied. This innovative idea requires a substantial internal volume for granular beads to achieve a sufficient stiffness. The mechanism is unlikely to adopt a compact design that spares a hollow passage for MIS instruments. To overcome this problem, several other jamming methods have been proposed. The layer jamming mechanism [15], [16] is capable of tuning the manipulator stiffness by making use of the controllable friction between the multi-layer skins by changing the layer-wise air pressure. Similar concepts using different mediums have been proposed [17], [18]. Zhong *et al.* [19] designed a bi-stable rigid joint for a soft robot to produce a locking mechanism for stiffness variation. The aforementioned solutions innovate from the perspective of robot design, which require fabrications of complicated continuum robot prototypes. Nevertheless, the adjustable-rigidity soft robots can be realized using pure actuation methods. Shiva *et al.* [23] proposed an approach to control the stiffness of a silicone-based pneumatically driven soft robot by actuating the vine-like tendons that adhere to the outer layer in an antagonistic way, opposing the pneumatic actuation. The hybrid actuation scheme allows one to control the robot pose and stiffness simultaneously. However, it is a common limitation that the pneumatic-driven soft robots are having a relatively large diameter (⌀23 mm in [23], ⌀32 mm in [24]) as they need bulky air chambers for pressurization [2].

Changing the gap or spacing within the robot structure through the tendon/cable-driven mechanism is an alternative to downsize the variable-stiffness continuum manipulator [24]. In [22], a pure cable-driven continuum robot based on stacking of multiple rigid arched disks was capable of tuning its stiffness by tensioning the cables along with the robot asymmetrically. Tamadon *et al.* [20] developed a rigid-bodied continuum manipulator for implant delivery in cardiac valve delivery. The ⌀28 mm single-segment robot was featured with the functions of tip positioning and configuration locking by controlling the cable tension. Choset *et al.* [21] developed a highly articulated robotic probe (HARP), also a flexible device assembled using rigid components, which can be stiffened by cable-tensioning. Utilizing the cable-driven mechanism, they downscaled the diameter of the continuum probe to 12 mm. These cable-actuated manipulators allow compact designs with a hollow passage in a considerable volume (sizes of conventional laparoscopic surgical instruments varies from 3 to 5 mm [22]). For the ease of reading, we list some variable-stiffness continuum robots in Table I.

B. Contribution

During the operation, the continuum robot is often required to carry a load, leading to an additional deformation on the body. In order to retain the original pose, it is desired to adjust the stiffness with respect to the load. In this work, the stiffness adjustment on a two-segment soft robot is achieved through the tendon tensioning method. Compared with the aforementioned studies, our robot adopts a backboneless structure to improve the body deformability. As a result, the tensioning would improve the bending and axial stiffness to cancel out the load. The experiment results indicate that the current end-effector position and the robot configuration would affect the robot stiffness, increasing the challenges in evaluating the required stiffness based on the load. To overcome this problem, this work proposes a scheme to correlate the tendon forces, in the form of displacements, with the relative end-effector position. Based on the feedback from a depth camera, the required tension force is adaptively adjusted to compensate for the deviation that caused by the load. Experiments were conducted to verify that the proposed tendon-tensioning method can stiffen the overall soft manipulator from a soft state to a stiffened state without excessive deviation in the configuration. Different end-effector trajectories were examined to evaluate the tip positioning accuracy under various loads. This work extends our prior works that allows the configuration control of a dual-segment soft robot in a 2D space [25]. The contributions of this work are as follows:

- We develop a miniature soft-bodied dual-segment continuum manipulator with variable-stiffness. The variable-stiffness is realized by using the proposed tendon-tensioning control method, which benefits a compact robot design, and enables the soft robot to stabilize its planned motion by compensating for external forces.
- We propose a tendon-tensioning method that provides an additional DOF, the manipulator's stiffness, for control. The feasibility is supported by extensive experiments. By employing the eye-to-hand RGB-D visual sensing, the manipulator is capable of adaptively tuning its stiffness only depends on the spatial perception of the end-effector. Without quantifying the instantaneous stiffness, we contribute a generalized method for tuning the stiffness of the tendon-driven soft-bodied robots in the presence of external disturbances without onboard sensing.

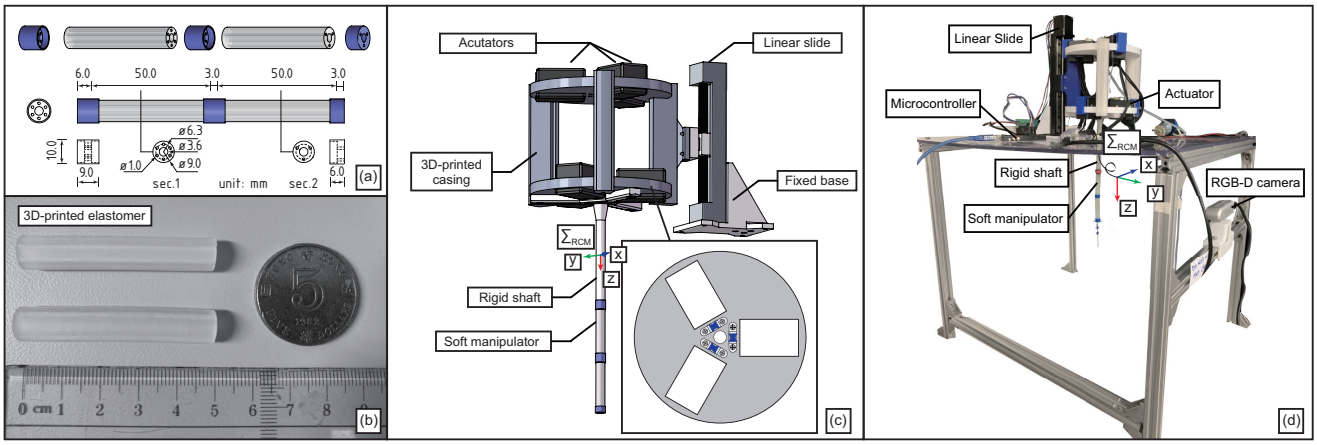

Fig. 2. (a) Design layout of the soft manipulator and its assembly. (b) Snapshot of 3D-printed soft segments. (c) Robot assembly. (d) Overall setup.

II. Prototype Description and Method

A. Prototype Description

The layout of our dual-segment soft robot and the stereolithography-based 3D-printed soft segments are demonstrated in Fig. 2(a) and Fig. 2(b). The soft body was made from Agilus30 (Stratasys Ltd., MN, USA) PolyJet photopolymer. The manipulator is composed of two different segments of the same size. The distal segment contains three equidistantly distributed passages for tendons, while the proximal segment has six in total. Each soft segment is 50 mm in length with an outer diameter of 9 mm. A ⌀3.6 mm lumen, which is adequate to fit an aspirator tube or a flexible endoscope, is reserved at the axial center. The soft manipulator was driven by six tendons that wired along the passages of the body and tied at the disks, and the total weight of the manipulator is 5.2 g. The assembly of the robot is shown in Fig. 2(c). To manipulate the robot, each tendon was connected to a Dynamixel XM430-W350 actuator (ROBOTIS, Seoul, Korea) through a fixed pulley, and these actuators were secured on a 3D-printed fixture. To provide an additional translational DOF, we mounted the fixture on a linear slide with its moving direction perpendicular to the ground. The translational DOF configures a remote center of motion (RCM) mechanism, which is widely used in R-MIS to physically bound the motion to a point to mechanically reduce the risk of tearing the incision port and gain higher dexterity [26], [27]. The details concerning the prototype can be found in our previous work [28] and the supplement video.

As depicted in Fig. 2(d), a depth camera (RealSense D435) was mounted at a side, forming an eye-to-hand system, to perceive the spatial position of the labeled points-of-interest (POIs). A Kanade–Lucas–Tomasi (KLT) tracker was employed to enhance the tracking stability of registered features in successive frames. In our case, the tracking system was hosted by a laptop with a 16GB RAM CPU, allowing real-time tracking at around 20 fps in 640×480p live stream. We set the world coordinate frame at a fixed spatial point as the origin of Σ_{RCM} which is 50 mm away from the base of the proximal soft segment when the translational DOF is at zero, with its $\hat{\mathbf{z}}$-axis points to the distal end and $\hat{\mathbf{y}}$-axis aligns toward the camera.

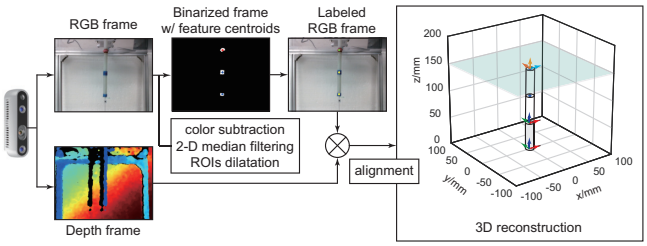

Fig. 3. RGB-D-based visual tracking and the manipulator's 3D reconstruction.

The coordinate of the end-effector with respect to (w.r.t.) Σ_{RCM} can be calculated by homogeneous matrix transformations. The frame-wise workflow of image processing is shown in Fig. 3. The hand-eye calibration was performed to reduce the mechanical and installation error. Images are enhanced for keypoint tracking. The resolution of the POIs is 0.001 mm on the X- and Z-axis (RGB module), and 1 mm on the Y-axis (depth module). The accuracy of image plane was within 0.1 mm, and that of the depth was $<$2% within 2 meters according to the camera specification. The tendon calibration was based on the 3D reconstruction and the default position of the POIs (base, intermediate, and tip position). The first step was to ensure that the aforementioned three points were aligned to the desired location as much as possible. After that, each cable was individually tested by actuating the same displacement, and the knots were manually adjusted to ensure symmetric robot motion in 6 directions.

B. Kinematics Modeling

Assumption: By following the tendon-driven mechanism as introduced in Sec. II-A, the robot kinematic model can be geometrically derived under the following assumptions:

- Each soft segment bends as a circular arc within a certain range [3], [29];
- Gravitational energy is neglected since the elastic potential energy dominates the gravity;
- Rigid disks are assumed to be infinitely thin, so that the distal end of the tendons are perpendicular to the disks;
- Actuation tendons are inextensible.

In a dual-segment continuum manipulator system, the actuator space $\boldsymbol{q}$ can be expressed by $\boldsymbol{q} = \begin{bmatrix}\boldsymbol{q}_1 & \boldsymbol{q}_2\end{bmatrix}^\intercal \in \mathbb{R}^{6\times 1}$, and the actuation for the k-th subsegment, where $k \in \{1, 2\}$, is $\boldsymbol{q}_k = \begin{bmatrix}q_{k,1} & q_{k,2} & q_{k,3}\end{bmatrix}^\intercal$, representing three actuation tendons for one segment. Without over deflection, a multi-segment continuum manipulator can be closely approximated by a finite set of consecutive constant curvatures geometrically in free space, which is widely known as piecewise constant curvature (PCC) assumption [3]. The PCC simplifies each segment to a 2-DOF system—each inextensible segment (L_k, a constant) can be bent on its own plane (θ_k), and a twist (ϕ_k) can be attained between neighboring segments (Fig. 4). For each segment, a twisting motion around its axial axis ($\hat{\mathbf{z}}_k$) which is not achievable by tendon actuation, is neglected. The abovementioned description concludes the spatial configuration of the k-th segment ($\boldsymbol{\psi}_k$) as $\boldsymbol{\psi}_k = \begin{bmatrix}\theta_k & \phi_k\end{bmatrix}^\intercal$, where $\theta_k \in [0, \theta_{\max}]$ and $\phi_k \in (-\pi, \pi]$. Therefore, the distal tip position of the k-th segment w.r.t. the $(k-1)$-th segment can be derived as

$$\boldsymbol{p}_k^{k-1} = \begin{bmatrix}\mathbf{x}_k \\ \mathbf{y}_k \\ \mathbf{z}_k\end{bmatrix} = \frac{L_k}{\theta_k}\begin{bmatrix}(1-c_{\theta_k})\,c_{\phi_k} \\ (1-c_{\theta_k})\,s_{\phi_k} \\ s_{\theta_k}\end{bmatrix} \tag{1}$$

where $c_{(\cdot)}$ and $s_{(\cdot)}$ are the abbreviations for $\cos(\cdot)$ and $\sin(\cdot)$, respectively. The configuration of the k-th segment w.r.t. its base ($\boldsymbol{\psi}_k$) can be derived from (1) as

$$\boldsymbol{\psi}_k = \begin{bmatrix}\theta_k \\ \phi_k\end{bmatrix} = \begin{bmatrix}2\arccos\frac{|\mathbf{z}_k|}{\|\boldsymbol{p}_k^{k-1}\|_2} \\ \arctan\frac{\mathbf{y}_k}{\mathbf{x}_k}\end{bmatrix}, \tag{2}$$

where $\|\cdot\|_2$ is the Euclidean norm. Under the assumption of inextensible tendons, one can geometrically (see Fig. 4(a)) define the relation between the specific tendon actuation ($q_{k,i}$) and the segment configuration ($\boldsymbol{\psi}_k$):

$$q_{k,i} = -\theta_k r c_{[\phi_k+(i-1)\xi]} \tag{3}$$

where $i \in \{1, 2, 3\}$ indicates the numbered tendon A, B, C, and $\xi = \frac{2\pi}{3}$ represents the trisection angle of circle. The negative sign notes a pulling (tensioning) motion. The radius of the tendon distribution is r. Taking the time derivative of (3) yields

$$\dot{\boldsymbol{q}}_k = \underbrace{\begin{bmatrix}-rc_{\phi_k} & r\theta_k s_{\phi_k} \\ -rc_{\phi_k+\xi} & r\theta_k s_{\phi_k+\xi} \\ -rc_{\phi_k+2\xi} & r\theta_k s_{\phi_k+2\xi}\end{bmatrix}}_{\mathbf{J}_{kq\psi}} \underbrace{\begin{bmatrix}\Delta\theta_k \\ \Delta\phi_k\end{bmatrix}}_{\dot{\boldsymbol{\psi}}_k} \tag{4}$$

where $\mathbf{J}_{kq\psi}$ is the Jacobian matrix that maps the actuation and configuration of the k-segment, and $\dot{\boldsymbol{\psi}}_k$ can be approximately treated as the change of (2) in instantaneous kinematics. It should be noted that

$$\sum_{i=1}^{3}\dot{q}_{k,i} = 0. \tag{5}$$

On the basis of (3), the mapping between tendon actuation and manipulator configuration can be attained as follows [3]:

$$\theta_k = \frac{2\sqrt{q_{k,1}^2 + q_{k,2}^2 + q_{k,3}^2 - q_{k,1}q_{k,2} - q_{k,1}q_{k,3} - q_{k,2}q_{k,3}}}{3r}, \tag{6}$$

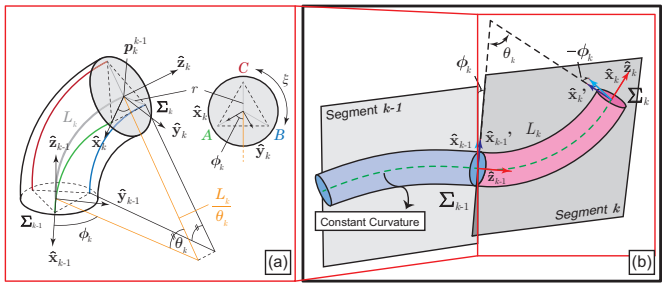

Fig. 4. Geometry assignment of the PCC model. (a) the k-th segment; (b) Consecutive segments of the k-th and the $(k-1)$-th.

$$\phi_k = \operatorname{atan2}\left(3\left(q_{k,2} - q_{k,3}\right), \sqrt{3}\left(q_{k,2} + q_{k,3} - 2q_{k,1}\right)\right) \tag{7}$$

where $\operatorname{atan2}(s_\phi, c_\phi)$ computes the four-quadrant inverse tangent of s_ϕ and c_ϕ such that $\phi \in (-\pi, \pi]$. To this end, the analytical solution of manipulator actuation to assigned tip pose can be ideally derived as $\boldsymbol{q}_k = f_{\text{inv}}\left(\boldsymbol{p}_k^{k-1}\right)$, in which $f_{\text{inv}}(\cdot)$ is the inverse mapping from the segment tip to the segment actuation in the k-th segment.

As demonstrated in Fig. 4, the orientation of the k-th segment tip w.r.t. its base is determined by three sequential rotations: (i) rotating ϕ_k around the $\hat{\mathbf{z}}_{k-1}$ axis, (ii) rotating θ_k around the $\hat{\mathbf{y}}_{k-1}$, (iii) rotating ϕ_k reversely around the $\hat{\mathbf{z}}_k$ axis of the current tip frame to ensure the torsionless assumption within each segment. Hence, the rotation matrix of the k-th segment ($\mathbf{R}_k^{k-1}$) can be expressed by

$$\begin{aligned}\mathbf{R}_k^{k-1} &= \operatorname{Rot}\left(\hat{\mathbf{z}}_{k-1}, \phi_k\right)\cdot\operatorname{Rot}\left(\hat{\mathbf{y}}_{k-1}, \theta_k\right)\cdot\operatorname{Rot}\left(\hat{\mathbf{z}}_k, -\phi_k\right) \\ &= \begin{bmatrix}c_{\phi_k}^2 c_{\theta_k} + s_{\phi_k}^2 & c_{\phi_k}s_{\phi_k}\left(c_{\theta_k}-1\right) & c_{\phi_k}s_{\theta_k} \\ c_{\phi_k}s_{\phi_k}\left(c_{\theta_k}-1\right) & s_{\phi_k}^2 c_{\theta_k} + c_{\phi_k}^2 & s_{\phi_k}s_{\theta_k} \\ -c_{\phi_k}s_{\theta_k} & -s_{\phi_k}s_{\theta_k} & c_{\theta_k}\end{bmatrix},\end{aligned} \tag{8}$$

where the operator $\operatorname{Rot}(\hat{\mathbf{u}}_k, \delta)$ denotes the rotation matrix of rotating angle (δ) along the unit axis of the k-th segment ($\hat{\mathbf{u}}_k$).

For our dual-segment manipulator system, we use the notation t for tip, m for middle-point (which is also the tip of the proximal segment), and b for base. The position of tip frame w.r.t. the stationary RCM can be obtained as

$$\boldsymbol{p}_t^{\text{RCM}} = \mathcal{H} + \boldsymbol{p}_m^b + \mathbf{R}_m^b\boldsymbol{p}_t^m \tag{9}$$

where $\mathcal{H} = \begin{bmatrix}0 & 0 & \boldsymbol{h}\end{bmatrix}^\intercal$ represents the translation DOF in axial direction w.r.t. the RCM.

C. Stiffness Variation

Natural soft tissue exhibit a self-protective mechanism against external forces exerted on the body: being soft at small strains, and rapidly stiffened at higher strains to prevent damage. In this work, we propose a *bioinspired* method that learns from such stress-stiffening behavior of natural soft tissues [30]. We employ this idea to contribute a variable-stiffness soft robot with a better control under large strains that caused by the external forces.

Assume the soft manipulator to be a virtual spring in free space with an initial stiffness of $\mathbf{K}_{\boldsymbol{q}}$ in response of the force

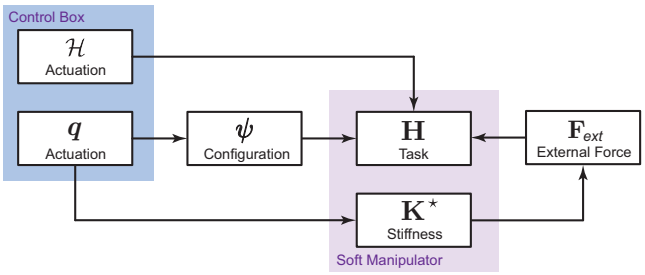

Fig. 5. The mapping of the proposed soft robot system. The actuation space is also responsible to the robot stiffness.

of tendons actuation $\mathbf{F}_{\boldsymbol{q}}$ and a resultant tip displacement $\boldsymbol{s}_{\boldsymbol{q}}$ in the task space, one gets

$$\mathbf{F}_{\boldsymbol{q}} = \mathbf{K}_{\boldsymbol{q}} \boldsymbol{s}_{\boldsymbol{q}}. \tag{10}$$

In the case where an external force, within the elastic limit of the soft robot, is introduced to the system, and the initial stiffness is not robust enough to resist, equation (10) shall be revised as

$$\mathbf{F}_{\boldsymbol{q}} + \mathbf{F}_{ext} = \mathbf{K}_{\boldsymbol{q}} \left(\boldsymbol{s}_{\boldsymbol{q}} + \Delta \boldsymbol{u} \right) \tag{11}$$

where $\mathbf{F}_{ext}$ is the external force that applied to the soft manipulator, and $\Delta \boldsymbol{u}$ is the undesired perturbation of the robot tip. The stiffness of the manipulator $\mathbf{K}_{\boldsymbol{q}}$ is an actuation dependent variable: intuitively, a bent segment will be stiffer than the straight segment. With respect to an arbitrary lateral-axial resolution, the external force can be explicitly expressed as

$$\mathbf{F}_{ext} = \begin{bmatrix} \mathbf{F}_{lt} \\ \mathbf{F}_{ax} \end{bmatrix} = \begin{bmatrix} K_{lt} & 0 \\ 0 & K_{ax} \end{bmatrix} \begin{bmatrix} \Delta \boldsymbol{u}_{lt} \\ \Delta \boldsymbol{u}_{ax} \end{bmatrix} = \mathbf{K}_{\boldsymbol{q}} \Delta \boldsymbol{u} \tag{12}$$

where $\Delta \boldsymbol{u}_{lt} = \|\mathbf{x}_{des}, \mathbf{y}_{des}\|_2 - \|\mathbf{x}_{cur}, \mathbf{y}_{cur}\|_2$ and $\Delta \boldsymbol{u}_{ax} = \|\mathbf{z}_{des}\|_2 - \|\mathbf{z}_{cur}\|_2$ represent the spatial deviation in the lateral and axial direction, respectively.

To compensate the perturbation, we apply extra force to the tendons, $\underline{\mathbf{F}}$, as a prestress to the system to obtain a new tip displacement $\underline{\boldsymbol{s}}$ by a displacement compensation of the tip $\Delta \boldsymbol{c}$:

$$\mathbf{F}_{\boldsymbol{q}} + \mathbf{F}_{ext} + \underline{\mathbf{F}} = \underbrace{\left(\mathbf{K}_{\boldsymbol{q}} + \underline{\mathbf{K}} \right)}_{\mathbf{K}^\star} \underbrace{\left(\boldsymbol{s}_{\boldsymbol{q}} + \Delta \boldsymbol{u} - \Delta \boldsymbol{c} \right)}_{\underline{\boldsymbol{s}}} \tag{13}$$

where $\underline{\mathbf{K}}$ is the additional stiffness matrix gained from the tendon prestress, and $\mathbf{K}^\star$ is the optimized manipulator stiffness. The mapping is given in Fig. 5. With the aim of having an accurate tip positioning control, one needs to narrow down the tip error which is defined by $\|\boldsymbol{s}_{\boldsymbol{q}} - \underline{\boldsymbol{s}}\|$. Minimizing such error formulates an optimization problem as

$$\arg\min_{\underline{\mathbf{F}}} \left\| \frac{\mathbf{F}_{\boldsymbol{q}}}{\mathbf{K}^\star - \underline{\mathbf{K}}} - \frac{\mathbf{F}_{\boldsymbol{q}} + \mathbf{F}_{ext} + \underline{\mathbf{F}}}{\mathbf{K}^\star} \right\|. \tag{14}$$

It has been experimentally found that the mechanical response of the soft elastomer we use is highly nonlinear, and it could be affected by the 3D printing parameters such as build orientation [31]. Therefore, it is challenging to precisely formulate a relationship between the tendon actuation and the manipulator's strain. In addition, the external force is usually unknown when without onboard sensors (such as tension sensors [32] for tendon, or strain gauges [33] that adhered/embedded to the soft body). However, with a depth vision provided by the RGB-D camera, the spatial deviation of the POIs ($\Delta \boldsymbol{u}$) can be easily acquired. The deviation of POIs can be obtained by other spatial positioning setups (e.g., EM tracking) as well.

Given the assumption that the tendons are inextensible, the actuation force that applied to the tendons can be linearly approximated by a non-zero positive constant α as

$$\begin{cases} \mathbf{F}_{\boldsymbol{q}} = \alpha \boldsymbol{q} \\ \underline{\mathbf{F}} = \alpha \underline{\boldsymbol{q}} \end{cases} \tag{15}$$

where $\underline{\boldsymbol{q}}$ denotes the extra tendon actuation in the form of pulling length. Therefore, equation (13) can be rewritten as

$$\begin{aligned} \alpha\left(\boldsymbol{q} + \underline{\boldsymbol{q}}\right) &= \left(\mathbf{K}_{\boldsymbol{q}} + \underline{\mathbf{K}} \right) \left(\boldsymbol{s}_{\boldsymbol{q}} + \Delta \boldsymbol{u} - \Delta \boldsymbol{c} \right) - \mathbf{K}_{\boldsymbol{q}} \Delta \boldsymbol{u} \\ &= \mathbf{K}_{\boldsymbol{q}} \boldsymbol{s}_{\boldsymbol{q}} - \mathbf{K}_{\boldsymbol{q}} \Delta \boldsymbol{c} + \underline{\mathbf{K}} \boldsymbol{s}_{\boldsymbol{q}} + \underline{\mathbf{K}} \Delta \boldsymbol{u} - \underline{\mathbf{K}} \Delta \boldsymbol{c} \\ &= \mathbf{K}^\star \boldsymbol{s}_{\boldsymbol{q}} - \mathbf{K}^\star \Delta \boldsymbol{c} + \underline{\mathbf{K}} \Delta \boldsymbol{u}, \end{aligned} \tag{16}$$

where $\left(\boldsymbol{q} + \underline{\boldsymbol{q}}\right)$ denotes the superposition of the tendon actuation which can be termed as the optimized actuation $\boldsymbol{q}^\star$. Hence, it gives

$$\boldsymbol{q}^\star = \alpha^{-1} \left(\mathbf{K}^\star \boldsymbol{s}_{\boldsymbol{q}} - \mathbf{K}^\star \Delta \boldsymbol{c} + \underline{\mathbf{K}} \Delta \boldsymbol{u} \right). \tag{17}$$

On the RHS of (17), the first term $\alpha^{-1} \mathbf{K}^\star \boldsymbol{s}_{\boldsymbol{q}}$ represents the designated actuation with a resultant tip motion under optimized stiffness, the second term $-\alpha^{-1} \mathbf{K}^\star \Delta \boldsymbol{c}$ denotes the compensation of tip motion which is generated by optimized stiffness, and the third term $\alpha^{-1} \underline{\mathbf{K}} \Delta \boldsymbol{u}$ is the neglectable deviation which is arisen by the extra stiffness. If $\underline{\mathbf{K}} = 0$, the initial stiffness shall not provide any compensation and thus $\Delta \boldsymbol{c} = 0$, returning $\boldsymbol{q} = \alpha^{-1} \mathbf{K}_{\boldsymbol{q}} \boldsymbol{s}_{\boldsymbol{q}}$, which is the same as the elementary actuation given by (10). According to (17), we can regulate the optimized actuation of tendons. Using an iterative approach to update the actuation at the n-th node of the path, one can obtain

$$\underbrace{\boldsymbol{q}^\star}_{optimized} := \underbrace{\boldsymbol{q}}_{IK} - \underbrace{\int_0^n \operatorname{sgn}\left(\boldsymbol{p}_{t,des}^{\mathrm{RCM}} - \boldsymbol{p}_{t,cur}^{\mathrm{RCM}} \right) \lambda \mathcal{Q} \mathbf{I} \, \mathrm{d}n}_{stiffening\ term} \tag{18}$$

where $\boldsymbol{q}^\star \in \mathbb{R}^{6\times 1}$ represents the actuation being tuned, and $\boldsymbol{q} \in \mathbb{R}^{6\times 1}$ denotes the instantaneous inverse kinematic solution of desired tip pose. $\boldsymbol{p}_{t,\underline{\ }}^{\mathrm{RCM}}$ is the desired or current detected tip position w.r.t. the RCM frame. $\mathcal{Q}$ is the tensioning-loosening variable based on the depth visual feedback as

$$\mathcal{Q} = \mu \|\Delta \boldsymbol{u}\|_2, \quad 0 \leq \mathcal{Q} \leq \varepsilon \tag{19}$$

such that (5) becomes $\sum_{i=1}^{3} \dot{q}_{k,i}^\star = \text{const.}$, with (6) and (7) still hold, ensuring the robot configuration will not be changed when updating $\boldsymbol{q}^\star$ (will be experimentally examined in Sec. III-A). We empirically set μ as 0.05 based on the incremental motion of the servo motors. And $\mathbf{I} = \begin{bmatrix} 1 & 1 & 1 & \frac{1}{2} & \frac{1}{2} & \frac{1}{2} \end{bmatrix}^\mathsf{T}$ is the column vector representing the decoupled actuation tendons for dual-segment robot. Recalling equation (4), the total Jacobian matrix can be assembled as

$$\mathbf{J}_{q\psi} = \underbrace{\begin{bmatrix} \mathbf{e}_3 & \mathbf{e}_3 \\ \mathbf{e}_3 & \mathbf{0} \end{bmatrix}}_{\mathcal{A}} \begin{bmatrix} \mathbf{J}_{1q\psi} & \mathbf{0} \\ \mathbf{0} & \mathbf{J}_{2q\psi} \end{bmatrix} \in \mathbb{R}^{6\times 4} \tag{20}$$

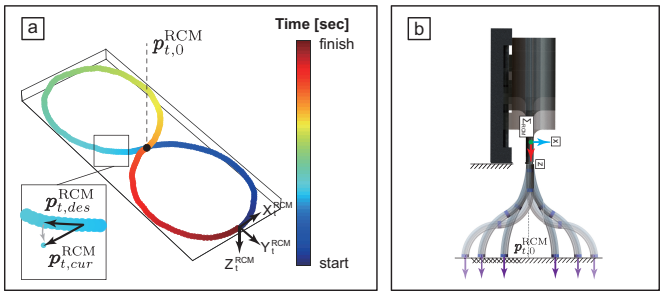

Fig. 6. (a) A typical closed trajectory. (b) Opposite-bending configuration for tip motion decoupling [28].

Algorithm 1: Adaptive stiffness by tuning tension

Result: $\boldsymbol{q}^{\star}$
Initialize $\boldsymbol{\varepsilon}$, μ, $\mathcal{P}_{\text{traj}} \in \mathbb{R}^{3N}$;
Track $\boldsymbol{p}_{t,cur}$ from RGB-D;
$n = 1$;
$\boldsymbol{q}^{\star} = \mathbf{0}$;
while $n \leq N$ **do**
  $\boldsymbol{p}_{t,des} = \mathcal{P}_{\text{traj}}(:, n)$;
  $\boldsymbol{q} = f_{\text{inv}}(\boldsymbol{p}_{t,des})$;
  if $\boldsymbol{q}^{\star} \in [\boldsymbol{q}_{lowerlimit}, \boldsymbol{q}_{upperlimit}) == 1$ **then**
    if $\|\boldsymbol{p}_{t,des} - \boldsymbol{p}_{t,cur}\|_2 > \boldsymbol{\varepsilon}$ **then**
      get $\boldsymbol{q}^{\star}$ from Eq. (18);
  $n := n + 1$;

where $\mathcal{A}$ represents the actuation coupling matrix between segments, and $\mathbf{e}_3$ denotes the 3-by-3 identity matrix for the Jacobian coupling. The pose of the proximal segment shall be corrected together with the distal segment when the distal tip is changing its position through actuating the distal cables that running through the proximal segment [28]. A buffer scalar λ is assigned to the tensioning term for a smoother transition of the change of stiffness. To determine whether the current state of the manipulator shall be stiffened or loosened, a position-based switch was designed as shown in Fig. 6(a) and algorithm 1 based on (21):

$$\operatorname{sgn}\left(\boldsymbol{p}_{t,des}^{\text{RCM}} - \boldsymbol{p}_{t,cur}^{\text{RCM}}\right) \begin{cases} > 0, & \text{stiffen} \\ = 0, & \text{maintain} \\ < 0, & \text{loosen.} \end{cases} \tag{21}$$

When the sign operation returns positive, the tension applied to the soft robot shall be enhanced so as to stiffen the robot to compensate for the deviation from the desired path. On the contrary, the tendons shall be loosened to reduce the overshooting of stiffening, as exceeding tendon actuation would induce noticeable strain along the manipulator's neutral line. With a continuous path $\mathcal{P}_{\text{traj}}$ defined by N nodes, one can update the actuation for each node based on the actuation computed from inverse kinematics. The tip positioning shall be gradually converged to the desired path within a threshold after several loops, depending on the setting. A tendon protection mechanism was set by defining the actuation limits. Once it was triggered, the update would be skipped to prevent the exceeding actuation which may break the tendons.

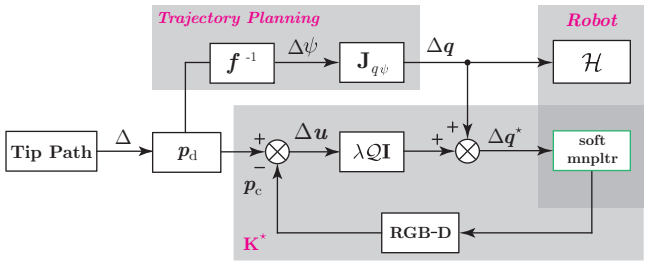

Fig. 7. Block diagram of the stiffness controller for open-loop trajectory tracking tasks.

D. Stiffness Control using Depth Visual Feedback

Tuning the stiffness based on the visual feedback allows the soft manipulator to automatically adjust its stiffness according to the effect caused by the unknown external force at different positions. Based on this understanding, we developed a depth vision-based method that enables the manipulator to variate its stiffness automatically in a 3D workspace according to the vectored perturbation of the tip position. The baseline pose, i.e., the desired pose ($\boldsymbol{p}_d^{\text{RCM}}$), to be compared with is the pose generated from the PCC model.

In end-effector trajectory planning, the user intuitively tends to assign path on a planar work surface, which yields $\boldsymbol{p}_t^{\text{RCM}} = [\mathbf{x}_t^b, \mathbf{y}_t^b, \epsilon]^{\intercal}$, where $\epsilon = \mathbf{z}_t^b + \boldsymbol{h}$ represents a constant related to the definition of works surface w.r.t. the RCM. Taking the advantage of our two-segment robot design, a special opposite-bending configuration (see Fig. 6(b)) is employed to decouple the tip position and orientation. The configuration shall be confined to (i) $\theta_1 = \theta_2$ where $\theta_k \in (0, \theta_{\max}]$, and (ii) $\phi_2 = \phi_1 - \operatorname{sgn}(\phi_1)\pi$ where $\phi_1 \in (-\pi, \pi]$, so that the distal tip can maintain its pointing direction vertically downward in an S-shape posture without losing the mobility in 3D [28]. The vertically downward pose benefits better stability in the presence of axial loads (see Sec. III-A), and provides a practical configuration to be used in R-MIS manipulation, such as blood aspiration and surgical site cleaning [28]. A depth vision-based controller was designed, as shown in Fig. 7, to compute the needed compensation actuation for the robot to conduct planar trajectory tracking with an adaptive stiffness. Therefore, the trajectory planning in the initial tendon actuation and the insertion-retraction stage followed an open-loop control, while the stiffness of the soft manipulator adopted the proposed closed-loop tendon-tensioning control based on the depth visual feedback. The corresponding experiments are illustrated in Sec. III-B.

III. Experiment

A. Validation of the Stiffening Scheme

In order to examine the change in axial stiffness ($\mathbf{K}_{ax}$), we introduce static load to the robot tip. The basic setup of our testbed is shown in Fig. 2(d). In the experiment, an axial load was given to the manipulator through metal weight. The axial stiffness should be optimized to bear the weight, and thus, the manipulator can maintain the desired pose. As shown in Fig. 8, the relationship between the tendon actuation and the axial force was plotted. The tip was initially configured at a certain

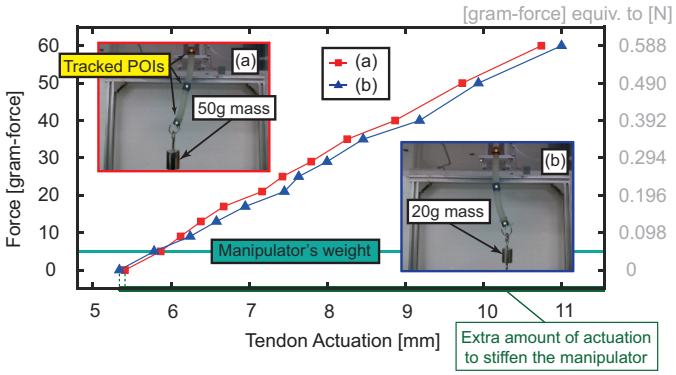

Fig. 8. The manipulator was stiffened by over-actuated tendons according to different loads such that the tip can maintain the spatial position of (a) $\boldsymbol{p}_t^{\text{RCM}} \approx [-12, 0, 148]^\intercal$, and (b) $\boldsymbol{p}_t^{\text{RCM}} \approx [12, 0, 148]^\intercal$ (unit: mm). The extra amount of tendon actuation represents the additional required tendon displacement that can stiffen the manipulator on top of configuring it to the desired pose.

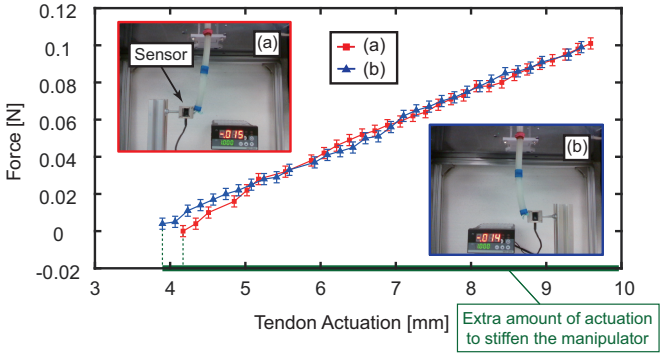

Fig. 9. Lateral pushing force measurement when the robot tendons were over-actuated. The error-bar represents the measurement error of force sensor, which is 0.3%.

position. Then, metals were hooked at the tip, generating an axial force from 5 to 60 gram-force, to deflect the tip position. The robot body was manually stiffened by applying extra tendon actuation so that the tip can maintain its initial position. The 3D coordinates of POIs were automatically tracked in real-time using an RGB-D camera. The result indicates a linear relationship between the tendon actuation and axial load. For lateral stiffness ($\mathbf{K}_{lt}$), we let the configured manipulator to resist a slight offset that caused by a force sensor (ZNLBS-VII-500, Ahznsensor Ltd., Anhui, China) such that the lateral force can be measured as a compressive force. The force sensor has a measurement range of $\pm$5N along its sensing axis with 0.001N resolution. Figure 9 indicates that the manipulator could generate a force laterally without changing its configuration, but under extra amount of tendon actuation. The result indicates a linear relationship between tendon actuation and measured force. The stiffening mechanism is established on the assumption that the extra tendon actuation—compared to the inversely computed actuation according to the task space—would cause a minor axial compression that is imperceptible.

Besides, we examined how different initial configuration and axial payload can affect the end-effector positioning in response of the extra actuation for stiffening (see the result in Fig. 10). In the experiment, the soft robot was posed in

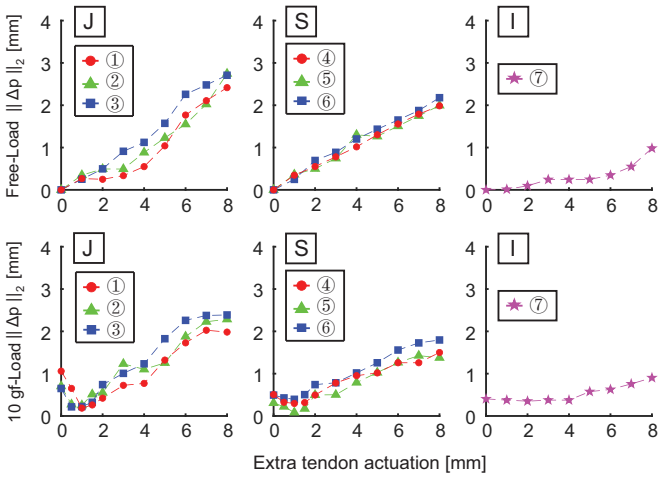

Fig. 10. The deviation of tip position affected by the proposed tendon tensioning method w.r.t. the desired position. The first row are in free-load, and the second row are loaded with a 10 gram axial force at the tip. Different initial configurations are considered, including the J-shape, S-shape, and I-shape (i.e., straight). Initial tip position are $\boldsymbol{p}_t^{\text{RCM}}$: ①$\approx [-11.7, -2, 144.9]^\intercal$ ②$\approx [-16.8, -6, 143.4]^\intercal$ ③$\approx [-13.6, -3, 143.9]^\intercal$ ④$\approx [-11.5, 7, 144.3]^\intercal$ ⑤$\approx [13.2, 7, 143.8]^\intercal$ ⑥$\approx [3.5, 5, 145.3]^\intercal$ ⑦$\approx [-1.628, 1, 145.8]^\intercal$ (unit: mm).

different initial shapes including J-, S-, and I-configuration. Extra tendon actuation (from 1–8 mm) was applied to the tendons to stiffen the robot. An RGB-D camera was used to measure the deviation of tip position from its desired one under both free-load and 10-gram load. All cases show a slight tip positioning error within 3 mm in Euclidean distance. The S-pose performs less error than that of the J-shape, and the straight pose demonstrates the least change. The loaded cases depict smaller errors than the free-loaded cases under the same configuration since the axial load (that axially scratching the robot) can partially cancel out the tendon actuation that axially compressing the manipulator. The results show that the optimal extra tendon actuation that can lower the tip positioning error falls in the range of $[0, 2]$ mm. Within a reasonable limit, the proposed stiffening method would not generate a major tip positioning error of our soft-bodied robot prototype. The minor error can be even smaller in the S-pose and I-pose. In particular, we further examined the spatial deviation of end-effector subjected to different axial payload when it is at the initial configuration of 'S-'. As depicted in Fig. 11, we gradually added the axial load at the robot tip in different amount of extra tendon actuation with its initial tip position at $\boldsymbol{p}_t^{\text{RCM}} = [11.05, 1, 144.57]^\intercal$. A higher level of tensioning, i.e., a stiffer soft robot body, demonstrates a better performance to resist the external force.

Based on the prototype experiment, Fig.12(a) investigates the relationship between the distance of the end-effector to the working surface center (perpendicular to the Z-axis of RCM) and the needed minimum extra tendon actuation to maintain such distant position in different payload conditions. For the ease of understanding, a schematic diagram is given in Fig.12(b) by simulation. The result indicates a nonlinear correlation among these 3 variants. When the desired position is farther away from the center (larger path), the soft ma-

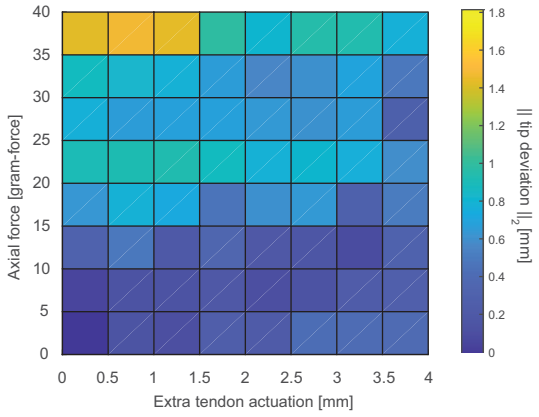

Fig. 11. Deviation map of the end-effector under different payload with extra tendon actuation. Upper left corner: without the tendon-tensioning stiffness adjustment, the axial force would generate large error of the tip. Upper right: with the tendon-tensioning stiffness adjustment, the error would be reduced. Lower right: the method will not generate major error.

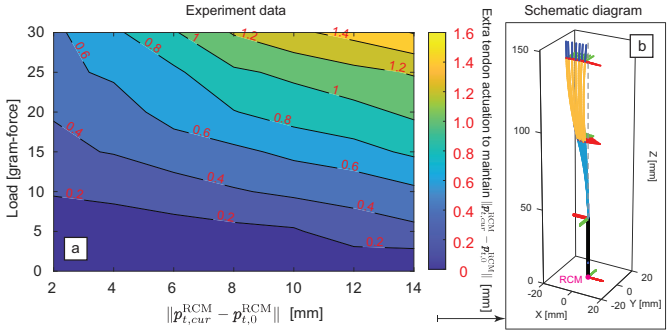

Fig. 12. (a) Mapping between the distance of the end-effector to the center and the corresponding minimum extra tendon actuation for stiffening the robot to maintain the desired tip position in different payload conditions. (b) Schematic diagram of the experiment.

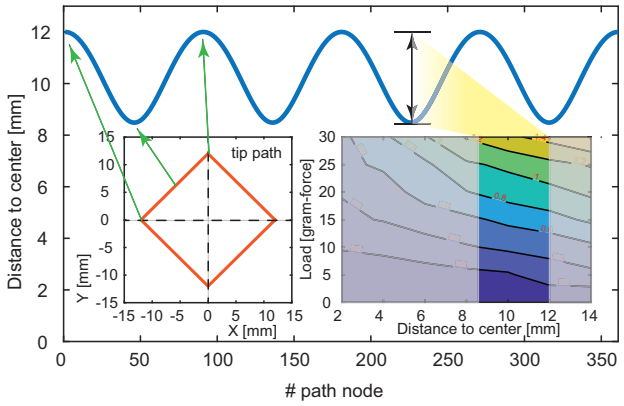

Fig. 13. An example of path distance to the working plane center. It necessitates different stiffness to maintain the tip position along the tracking in different payload condition.

nipulator is more sensitive to the disturbance, so that larger compensation would be required to maintain the position. In a trajectory tracking task, when the desired path is not a circle (i.e., not every point shares the same distance to the center), the minimum tendon compensation shall be iteratively updated. An example of tip path tracking is given in Fig. 13, where the

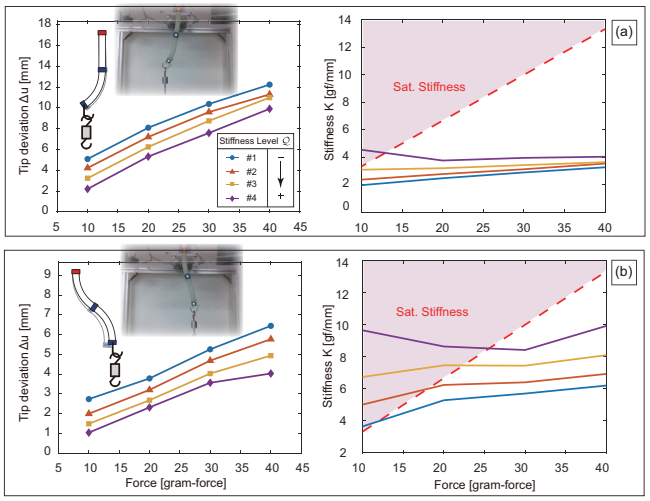

Fig. 14. The initial positions of the tip are: (a) $\boldsymbol{p}_t^{\mathrm{RCM}} = [-19.284, 0, 145.097]^\intercal$ (b) $\boldsymbol{p}_t^{\mathrm{RCM}} = [13.725, 0, 148.014]^\intercal$ (unit: mm). The right column figures plot the correlation between manipulator stiffnesses and static forces, where the reddish regions represent the 'satisfactory' stiffnesses that allow a tip perturbation within 3 mm.

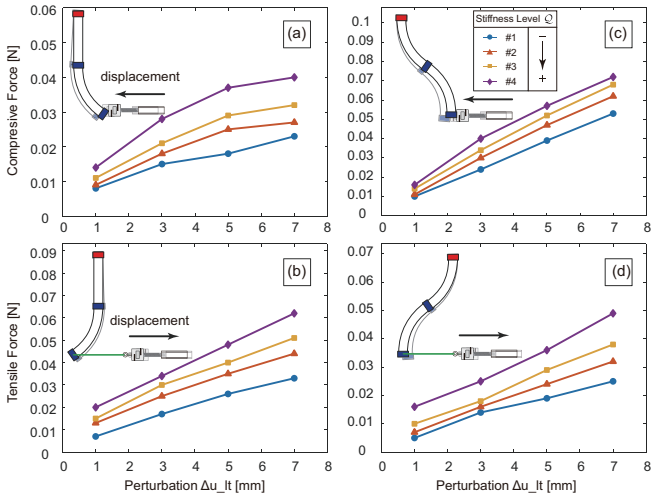

Fig. 15. The probe was mounted on a motor-driven linear slide. The lateral force was generally increased when the manipulator was stiffened, implying that the soft robot can be hardened in the lateral direction. ((a)–(d))

desired path is a square isometrically divided by 360 nodes. Without prior knowledge of the load, the required actuation for optimal stiffness is changing along with the change of the tip position. Therefore, it necessitates the closed-loop control for the tendon compensation for variable-stiffness.

To show the axial stiffening by tendon tensioning in different configurations, metal weights were hooked at the robot tip to deviate the tip positioning under different stiffness levels. As shown in Fig. 14, we measured the tip perturbation under four stiffness levels using four loads. The Hooke's law implies that the perturbation can be infinitesimal when the stiffness is infinite, i.e., completely rigid. Therefore, we set a satisfactory tip deviation of 3 mm based on the sensitivity of the depth vision and correlated a satisfactory stiffness that can correct the robot tip to its original position. The results show that

- the robot stiffness can be enhanced by synergistically

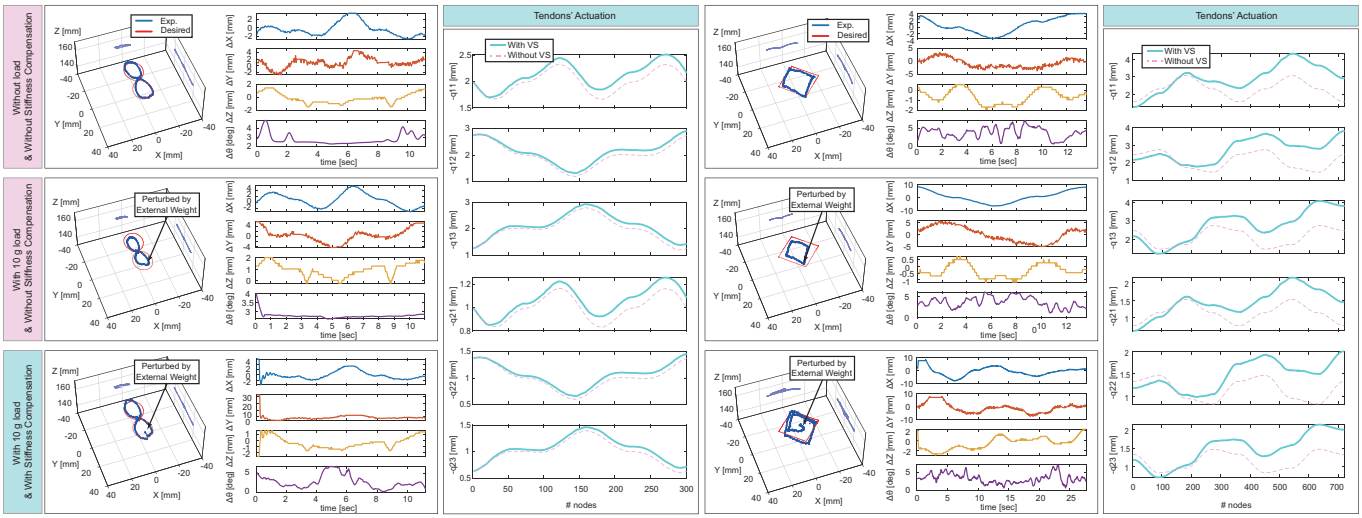

Fig. 16. Trajectory tracking performances of the open-loop control in free load (first row) and in 10 g load (second row), and with variable-stiffness control in 10 g load (third row).

tensioning the tendons;

- a stiffer rigidity mode shares a larger overlapped range with the satisfactory stiffness;
- the S-configurations exhibit higher stiffness than that of the J-configuration in the presence of axial load.

The results also indicate that the proposed method can stand alone from the robot task space to control the robot stiffness.

To demonstrate that the lateral stiffness can be tuned by tendon tensioning, we mounted a force sensor at the tip of a home-made probe which was secured on a motor-driven linear slide to perturb the configured manipulator (i.e., in different configurations such as J- or S-shape) by a known displacement with different tensioning mode and collected the compressive force data. Likewise, another demonstration of tuning lateral stiffness was conducted by reading tensile force, where the robot tip and the sensor were connected by a fishing line, and a known displacement, opposing to the direction of the previous test, was given to the slide such that the probe could measure the tensile force. The forces were recorded for every 2 mm perturbation from 1 to 7 mm. The main idea was to stiffen the manipulator so that it would show more resistance against the perturbation. The results are plotted in Fig. 15, where different stiffening levels were applied to enhance the lateral stiffness with the initial configuration unchanged. The results confirm that the lateral stiffness can be enhanced from the initial actuation by our presented tensioning method, and also justify the compliance nature of our variable-stiffness soft robot—it can be stiffened to a competent level for the manipulation purpose without losing the high-compliance to ensure the safety to the possible collision. This feature would be appreciated in the scene of human-robot interaction, such as R-MIS.

To this extent, the effectiveness of the proposed stiffening approach for the tendon-driven soft robot is validated. From Fig. 8 and Fig. 9, it can be seen that the measured force and tip deviation were not perfectly equally distributed even the robot was in a symmetrical motion, inferring that the stiffness of the soft body is subjected to various unquantifiable factors. It motivates the adoption of the closed-loop method to fine-tune the manipulator stiffness as described in Sec. II-D.

B. Tip Trajectory Tracking with Loading

With continuously defined waypoints for tip path and on the basis of Sec. II-D, the soft manipulator can perform tip trajectory tracking with a vision-based stiffness tuning when it is subjected to external loads.

Several experiments were conducted with an empirically-set trigger threshold of $\varepsilon = 3$ mm and buffer of $\lambda = 0.2$. The comparison of the performances of tracking different trajectories in different conditions are given in Fig. 16. It can be seen that when a payload was added to the manipulator, the operational trajectory would be deviated from its desired trajectory, and such deviation would be enlarged with increasing payload (Fig. 17). However, when utilizing the proposed stiffness compensation scheme, the tip could provide the tracking performances which were as good as that of the open-loop mode without payload. As shown in Fig. 17, the tracking performances were significantly improved especially with larger payloads. The method allows the robot to adjust its tendon actuation along the trajectory without knowing how much payload it was holding. The correction processes could be done within one trajectory loop. In the experiment, we conducted 3 trials for each trajectory in different payload condition (10, 20, and 30 gram-force), and collected the root-mean-square-error (RMSE) of tip positioning and angular deviation from the desired path (Table II). Supported by the experiment results, the average stiffness of the robot along the trajectory can be approximated using the force and position information ($\frac{\mathbf{K}^{*}-\mathbf{K}}{\mathbf{K}}$), and this method can enhance the stiffness by 132% for a square trajectory under an axial force of 30 gram-force. In addition, as shown in Fig. 18, experiment results indicate that the proposed method can be employed in tracking trajectory in different sizes accurately in loaded cases.

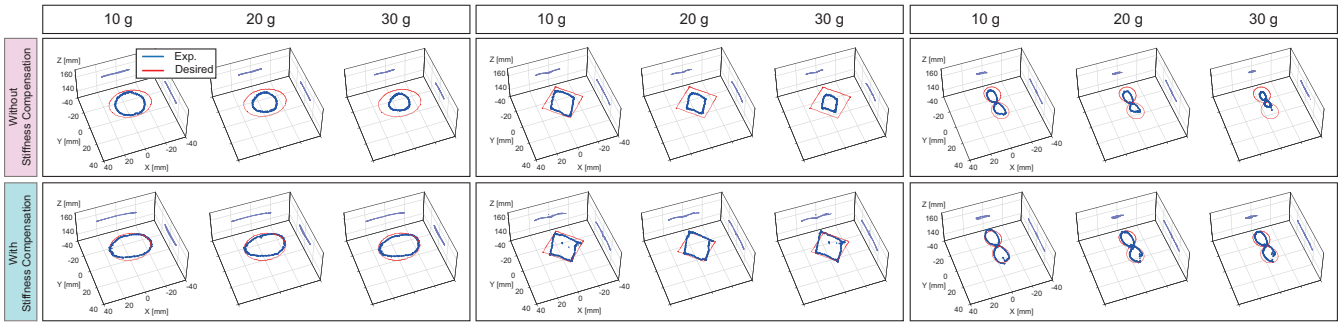

Fig. 17. Trajectory tracking performances of open-loop control (pink row) and with variable-stiffness control (green row) under different payload conditions.

TABLE II
RMSEs OF TRACKING DIFFERENT TRAJECTORIES (FIG. 17) IN 3 TRIALS

Tip Trajectory	⬭			□			∞		
Axial Load (gram-force)	10	20	30	10	20	30	10	20	30
RMSE of $\mathbf{x}_t^{\text{RCM}}$ (mm)	3.058 (4.964)	3.330 (6.305)	3.325 (7.389)	2.799 (4.831)	2.833 (6.234)	3.144 (7.201)	1.593 (2.313)	2.409 (2.633)	2.468 (3.331)
RMSE of $\mathbf{y}_t^{\text{RCM}}$ (mm)	3.170 (3.121)	2.890 (4.153)	2.870 (5.071)	2.740 (3.109)	2.361 (4.703)	2.245 (5.715)	2.689 (3.037)	2.510 (3.613)	3.220 (6.055)
RMSE of $\mathbf{z}_t^{\text{RCM}}$ (mm)	0.885 (0.969)	0.778 (1.369)	0.836 (1.656)	0.905 (0.614)	0.909 (0.829)	0.962 (1.011)	0.882 (0.579)	0.704 (0.726)	0.763 (1.391)
RMSE of Θ (°)	5.539 (3.148)	4.528 (2.688)	3.347 (2.579)	3.031 (3.970)	3.320 (3.589)	3.399 (3.489)	1.277 (3.393)	3.401 (2.345)	2.824 (1.814)
Stiffness Enhanced Avg. (%)	32.29	71.38	103.89	43.73	106.73	132.32	18.89	27.61	70.76

The values in bracket denote the reference values without stiffness compensation. The above trajectory shapes are in a size of 20 mm in either x- or y-axis.

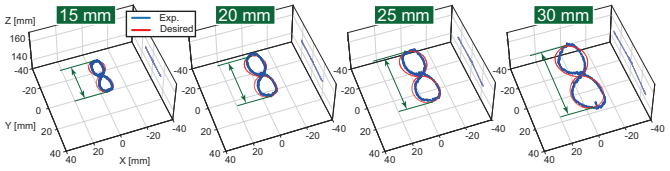

Fig. 18. Under the same axial force (10 gram-force), the stiffness-adaptiveness scheme fits well in different sizes of trajectory from 15 mm to 30 mm.

IV. DISCUSSION

This work innovates the soft-bodied robot with an additional degree of freedom by safely controlling its stiffness during the operational process. The proposed stiffening method demonstrates several advantages over the other manipulator stiffening methods/mechanisms that listed in Table I, including:

Applicability: Without complicated design and implementation of onboard sensors or specially-designed stiffening mechanism (e.g., stuffing granular, jamming, etc.), which makes our method rapidly applicable to many other existing tendon-driven soft robot systems with just an additional depth camera. The method provides an inexpensive solution to upgrade many existing soft robots to variable-stiffness versions.

Continuity: The method is applicable in some common scenarios where the closed-loop feedback is not necessarily continuous. For instance, in R-MIS, the sensory feedback is not always available throughout the course of the closed-loop manipulation. In conventional visual servoing methods [34], [35], the system shall compute the visually-available error in each loop to ensure the closed-loop control. However, the Jacobian update could be disturbed in some critical cases where the vision is lacking continuity. Thus, it ought to be switched to the open-loop mode. When it switches to the open-loop control, it can eventually result in a large error in terms of tip positioning, and it can be even worse when the disturbances are introduced. In our method, the trajectory tracking task is based on an open-loop control while the robot stiffness is secured by the closed-loop visual feedback. The experiments in Sec. III-B illustrate that the stiffness was iteratively accumulated. Even though the vision was blocked, the manipulator can still work as it was on the correct track based on the latest-optimized actuation without large error.

Adaptivity: The stiffening method is result-based, which does not require prior knowledge of the external payload. Within the payload capacity, the robot could fine-tune its stiffness to adapt to the external force without excessive deflections. As depicted from the experimental results, the method would not result in an infiniteness of the stiffness. A balance of stiff-and-soft can be reached.

However, since the method requires the robot to be quasi-static, the momentum caused by introducing a weight to the manipulator when it was in motion would reduce the tip positioning accuracy. Therefore, a slower motion would be preferred. Besides, the method limits the stiffness variability to either the proximal segment or to the whole manipulator. Moreover, the tendon-driven mechanism without tendon-pushing does not allow the stiffness compensation for the external force that axially compresses the manipulator.

V. CONCLUSION

In this work, we propose a tendon-tensioning scheme to upgrade a normal dual-segment soft robot to a variable-stiffness version. It is experimentally confirmed that the proposed scheme can variate the stiffness of a soft robot, i.e, providing an additional controllable DOF to the robot, without apparent change in configuration. In the application of trajectory tracking, depth vision was employed to acquire the spatial deviation of the end-effector caused by an axial payload. The visual perception of the tip was treated as the closed-loop feedback for stiffness compensation. Utilizing our

method, the manipulator can stabilize its instantaneous configuration by adaptively controlling its stiffness without losing its compliance. Extensive experiments were conducted to verify the principle of the tendon-tensioning method, and the anti-disturbance performance was also evaluated through the real-time trajectory tracking tests by adhering different payloads to the robot tip. The results indicate a significant improvement in terms of load-bearing trajectory tracking compared to the pure open-loop version, with a stiffness controllability up to 132%. The positioning error can be reduced up to 50% when with an external payload of 30 gram-force. And it can be inferred that the reduction would be more notable with heavier loads. This work shows that soft-bodied robots are having a great potential for the application in the future R-MIS manipulation for safer human-robot interaction.

REFERENCES

[1] D. Rus and M. T. Tolley, "Design, fabrication and control of soft robots," *Nature*, vol. 521, no. 7553, pp. 467–475, 2015.

[2] J. Burgner-Kahrs *et al.*, "Continuum robots for medical applications: A survey," *IEEE Trans. Robot.*, vol. 31, no. 6, pp. 1261–1280, 2015.

[3] R. J. Webster III and B. A. Jones, "Design and kinematic modeling of constant curvature continuum robots: A review," *Int. J. Robot. Res.*, vol. 29, no. 13, pp. 1661–1683, 2010.

[4] M. Mahvash and P. E. Dupont, "Stiffness control of surgical continuum manipulators," *IEEE Trans. Robot.*, vol. 27, no. 2, pp. 334–345, 2011.

[5] C. Li *et al.*, "Flexible robot with variable stiffness in transoral surgery," *IEEE/ASME Trans. Mechatron.*, vol. 25, no. 1, pp. 1–10, 2019.

[6] B. Ouyang *et al.*, "Robust model-predictive deformation control of a soft object by using a flexible continuum robot," in *Proc. IEEE/RSJ Int. Conf. Intell. Robot. Syst. (IROS)*, 2018, pp. 613–618.

[7] L. Blanc *et al.*, "Flexible medical devices: review of controllable stiffness solutions," *Actuators*, vol. 6, no. 3, p. 23, 2017.

[8] S. P. Timoshenko and J. M. Gere, *Theory of elastic stability*. Courier Corporation, 2009.

[9] J. Shintake *et al.*, "Variable stiffness actuator for soft robotics using dielectric elastomer and low-melting-point alloy," in *Proc. IEEE/RSJ Int. Conf. Intell. Robot. Syst. (IROS)*, 2015, pp. 1097–1102.

[10] A. Lendlein and R. Langer, "Biodegradable, elastic shape-memory polymers for potential biomedical applications," *Science*, vol. 296, no. 5573, pp. 1673–1676, 2002.

[11] J. Peters *et al.*, "Actuation and stiffening in fluid-driven soft robots using low-melting-point material," in *Proc. IEEE/RSJ Int. Conf. Intell. Robot. Syst. (IROS)*, 2019, pp. 4692–4698.

[12] A. Jiang *et al.*, "Robotic granular jamming: Does the membrane matter?" *Soft Robot.*, vol. 1, no. 3, pp. 192–201, 2014.

[13] M. Brancadoro *et al.*, "Fiber jamming transition as a stiffening mechanism for soft robotics," *Soft Robot.*, ahead of print. 2020.

[14] T. Ranzani *et al.*, "A soft modular manipulator for minimally invasive surgery: design and characterization of a single module," *IEEE Trans. Robot.*, vol. 32, no. 1, pp. 187–200, 2016.

[15] Y.-J. Kim *et al.*, "A novel layer jamming mechanism with tunable stiffness capability for minimally invasive surgery," *IEEE Trans. Robot.*, vol. 29, no. 4, pp. 1031–1042, 2013.

[16] T. Wang *et al.*, "Electrostatic layer jamming variable stiffness for soft robotics," *IEEE/ASME Trans. Mechatron.*, vol. 24, no. 2, pp. 424–433, 2019.

[17] A. Stilli *et al.*, "A novel concept for safe, stiffness-controllable robot links," *Soft Robot.*, vol. 4, no. 1, pp. 16–22, 2017.

[18] A. J. Loeve *et al.*, "Endoscope shaft-rigidity control mechanism:"forguide"," *IEEE Trans. Biomed. Eng.*, vol. 59, no. 2, pp. 542–551, 2011.

[19] Y. Zhong *et al.*, "Investigation on a new approach for designing articulated soft robots with discrete variable stiffness," *IEEE/ASME Trans. Mechatron.*, pp. 1–1, 2021.

[20] I. Tamadon *et al.*, "Positioning and stiffening of an articulated/continuum manipulator for implant delivery in minimally invasive surgery," *Int. J. Med. Robot. Comput. Assist. Surg.*, vol. 16, no. 2, p. e2072, 2020.

[21] A. Degani *et al.*, "Highly articulated robotic probe for minimally invasive surgery," in *Proc. IEEE Int. Conf. Robot. Automat. (ICRA)*, 2006, pp. 4167–4172.

[22] Y.-J. Kim *et al.*, "A stiffness-adjustable hyperredundant manipulator using a variable neutral-line mechanism for minimally invasive surgery," *IEEE Trans. Robot.*, vol. 30, no. 2, pp. 382–395, 2013.

[23] A. Shiva *et al.*, "Tendon-based stiffening for a pneumatically actuated soft manipulator," *IEEE Robot. Autom. Lett.*, vol. 1, no. 2, pp. 632–637, 2016.

[24] M. Cianchetti *et al.*, "Soft robotics technologies to address shortcomings in today's minimally invasive surgery: the stiff-flop approach," *Soft Robot.*, vol. 1, no. 2, pp. 122–131, 2014.

[25] J. Lai *et al.*, "Toward vision-based adaptive configuring of a bidirectional two-segment soft continuum manipulator," in *Proc. IEEE/ASME Int. Conf. Adv. Intell. Mechatron. (AIM)*, 2020, pp. 934–939.

[26] T. Kato *et al.*, "Tendon-driven continuum robot for endoscopic surgery: Preclinical development and validation of a tension propagation model," *IEEE/ASME Trans. Mechatron.*, vol. 20, no. 5, pp. 2252–2263, 2014.

[27] J. Ding *et al.*, "Design and coordination kinematics of an insertable robotic effectors platform for single-port access surgery," *IEEE/ASME Trans. Mechatron.*, vol. 18, no. 5, pp. 1612–1624, 2012.

[28] J. Lai *et al.*, "Verticalized-tip trajectory tracking of a 3d-printable soft continuum soft robot: Enabling surgical blood suction automation," under review. 2020.

[29] K. Xu and N. Simaan, "An investigation of the intrinsic force sensing capabilities of continuum robots," *IEEE Trans. Robot.*, vol. 24, no. 3, pp. 576–587, 2008.

[30] D. Zhalmuratova and H.-J. Chung, "Reinforced gels and elastomers for biomedical and soft robotics applications," *ACS Appl. Polym. Mater.*, vol. 2, no. 3, pp. 1073–1091, 2020.

[31] F. F. Abayazid and M. Ghajari, "Material characterisation of additively manufactured elastomers at different strain rates and build orientations," *Addit. Manuf.*, p. 101160, 2020.

[32] M. C. Yip and D. B. Camarillo, "Model-less feedback control of continuum manipulators in constrained environments," *IEEE Trans. Robot.*, vol. 30, no. 4, pp. 880–889, 2014.

[33] H. Wang *et al.*, "Toward perceptive soft robots: Progress and challenges," *Adv. Sci.*, vol. 5, no. 9, p. 1800541, 2018.

[34] H. Wang *et al.*, "Visual servoing of soft robot manipulator in constrained environments with an adaptive controller," *IEEE/ASME Trans. Mechatron.*, vol. 22, no. 1, pp. 41–50, 2016.

[35] F. Xu *et al.*, "Underwater dynamic visual servoing for a soft robot arm with online distortion correction," *IEEE/ASME Trans. Mechatron.*, vol. 24, no. 3, pp. 979–989, 2019.

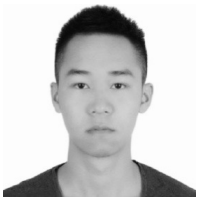

Jiewen Lai (S'20) received the B.Eng. degree in metallurgical engineering from Wuhan University of Science and Technology, Wuhan, China, in 2016, and the M.Sc. degree in mechanical and automation engineering from The Chinese University of Hong Kong, Hong Kong, in 2017. He is currently working toward the Ph.D. degree in mechanical engineering with The Hong Kong Polytechnic University, Hong Kong. His research interests include soft/continuum robot and surgical robot system.

Bo Lu received the B.Eng. degree in ship and offshore engineering from Dalian University of Technology, Dalian, China, in 2013, and the M.S. and Ph.D. degrees in mechanical engineering from The Hong Kong Polytechnic University, Hong Kong, in 2015 and 2019, respectively.

He is currently a Post-Doctoral Research Fellow with the T Stone Robotics Institute, The Chinese University of Hong Kong, Hong Kong. His current research interests include medical robotics, computer vision, and surgical automation technique.

Henry K. Chu (M'12) received the B.S. degree in mechanical engineering from the University of Waterloo, Waterloo, ON, Canada, and the M.S. and Ph.D. degrees in mechanical and industrial engineering from the University of Toronto, Toronto, ON, Canada.

He was a Post-Doctoral Fellow with the University of Toronto and the City University of Hong Kong, Hong Kong. He is currently an Assistant Professor with The Hong Kong Polytechnic University, Hong Kong. His research interests include robotic manipulation, vision-based control and automation, micro-system design, and tissue engineering.